

ACCURATE AND EFFICIENT BOUNDARY INTEGRAL METHODS FOR ELECTRIFIED LIQUID BRIDGE PROBLEMS*

DARKO VOLKOV[†], DEMETRIOS T. PAPAGEORGIU[†], AND PETER G. PETROPOULOS[†]

Abstract. We derive and implement boundary integral methods for axisymmetric liquid bridge problems in the presence of an axial electric field. The liquid bridge is bounded by solid parallel electrodes placed perpendicular to the axis of symmetry and held at a constant potential difference. The fluid is assumed to be nonconducting and has permittivity different from that of the passive surrounding medium. The problem reduces to the solution of two harmonic problems for the fluid and voltage potential inside the bridge and another harmonic problem for the voltage potential outside the bridge. The shape of the moving interface is determined by the imposition of stress, as well as kinematic and electric field boundary conditions, the former condition accounting for discontinuous electric stresses across the interface. We propose fast and highly accurate boundary integral methods based on fast summations of appropriate series representations of axisymmetric Green's functions in bounded geometries. We implement our method to calculate equilibrium shapes for electrified liquid bridges in the absence and presence of gravity. Such calculations appear in the literature using finite element methods, and our boundary integral approach is a fast and accurate alternative.

Key words. boundary integral method, Ewald's method, electrified liquid bridge, capillary instability

AMS subject classifications. 35J65, 74S15, 76B45, 76W05

DOI. 10.1137/040604352

1. Introduction. Flows containing moving interfaces where surface tension is present are of fundamental importance in different applications such as mixing and emulsification, printing and spraying, imaging, heat and mass transfer, and propulsion systems, to name a few. An important class of applications can be described by axisymmetric flows as in liquid jets or bridges, for instance. In cylindrical geometries, surface tension induces a long wave instability (this statement is a linear stability result—all wavy interfacial perturbations longer than the undisturbed jet circumference are unstable—see Plateau (1873) and Rayleigh (1878, 1892)) that leads to nonlinear dynamics, necking, and a topological transition. Mathematically, this event is a finite-time singularity of the three-dimensional axisymmetric Navier–Stokes equations in the presence of a free surface, and solution characteristics are mathematically and physically useful (see the reviews of Eggers (1997) and Papageorgiou (1995a, 1995b, 1996)). In fact, experiments agree with the theoretical solutions of highly viscous jets (see Papageorgiou (1995a)) extremely well and for times not too close to the singularity (see McKinley and Tripathi (2000)). Recent experiments have been performed to probe the fine details of the topological transition; see Rothert, Richter, and Rehberg (2001, 2003).

Full-scale simulations based on the Euler, Stokes, or Navier–Stokes equations are necessary in the general case. There is a vast literature on this subject, and of

*Received by the editors February 23, 2004; accepted for publication (in revised form) November 5, 2004; published electronically July 26, 2005.

<http://www.siam.org/journals/sisc/26-6/60435.html>

[†]Department of Mathematical Sciences and Center for Applied Mathematics and Statistics, New Jersey Institute of Technology, University Heights, Newark, NJ 07102 (darko.volkov@njit.edu, depapa@oak.njit.edu, peterp@m.njit.edu). The work of the first author was supported by National Science Foundation grant DMS-0072228. The work of the third author was supported in part by Air Force Office of Scientific Research grant F49620-02-1-0031.

particular interest to the present study are boundary integral methods. The reader is referred to recent reviews on inviscid and Hele–Shaw flows by Hou, Lowengrub, and Shelley (2001) and on Stokes flows by Pozrikidis (2001), as well as numerous references therein. The boundary integral methods developed herein are a first step in tackling singularity formation in liquid jets with either periodic boundary conditions or liquid bridges between parallel plates. In order to control the accuracy of the calculations, we choose to solve integral equations formulated over the fluid interface alone, and this requires the efficient calculation of series representations of the periodic or Dirichlet (Neumann) Green’s function. An alternative formulation is to distribute singularities on the bounding plates also, the advantage being that the free-space Green’s function can be used; see, for example, Gaudet, McKinley, and Stone (1996) for a Stokes flow study of an extending liquid bridge.

There have been several theoretical and experimental studies in the area of liquid bridges and the control of their stability by imposition of an axial electric field. In the theoretical arena, Gonzalez et al. (1989) considered the linear stability of electrified dielectric liquid bridges in the absence of gravity and demonstrated that an axial electric field can stabilize (at least in the linear regime) a bridge which would otherwise be unstable. They also performed experiments to confirm their findings. Residual gravity was introduced by Gonzalez and Castellanos (1993), and a similar stability analysis was carried out to determine local bifurcation diagrams near the zero gravity states. Of particular interest to the present study is that of Ramos and Castellanos (1993), who use finite element methods coupled with a Newton iteration to solve the static nonlinear problem of an electrified dielectric liquid bridge. Our boundary integral method does not require discretization of the flow field which extends radially to infinity. In a more recent linear stability study, Pelekasis, Economou, and Tsamopoulos (2001) calculate numerically stability curves from the generalized eigenvalue problem resulting from the finite element projection of the linear equations of dielectric and leaky dielectric viscous bridges, and they demonstrate clearly the stabilization effected by the electric field.

Experiments on the dynamics of electrified liquid bridges have been carried out by Burcham and Saville (2000) in a zero gravity environment, Gonzalez et al. (1989), and Ramos, Gonzalez, and Castellanos (1994). The latter two studies were performed in a terrestrial environment with gravity effects present. The electric field was found to stabilize the liquid bridge in the sense that equilibrium shapes could be achieved for longer bridges beyond the Plateau limit. Gravity breaks the midplane symmetry and produces amphora-like shapes which are thinner in the vicinity of the upper plate. Our numerical results are in full agreement with all the experimental findings.

2. The governing equations. Consider an axisymmetric liquid bridge of dimensional length $L/2$ held between two infinite parallel electrodes. The lower electrode is maintained at zero potential and the upper one at constant potential V_0 . In its undisturbed perfectly cylindrical state the bridge has a uniform circular cross section of radius R . The fluid is taken to be inviscid and incompressible of density ρ . Gravity is included, and surface tension acts and has constant coefficient σ . The fluid region (region 1) is nonconducting and has constant permittivity ε_1 , while the surrounding region (region 0) is dynamically passive, has constant permittivity ε_0 , and is nonconducting (e.g., air, as in the experiments; see the introduction). The problem geometry is sketched in Figure 1.

The problem is made dimensionless by scaling lengths with L , the pressure p by $\frac{\sigma}{R}$, fluid velocities \mathbf{u} by $(\frac{\sigma}{\rho R})^{1/2}$, time t with $(\frac{\rho R L^2}{\sigma})^{1/2}$, and voltage potential V

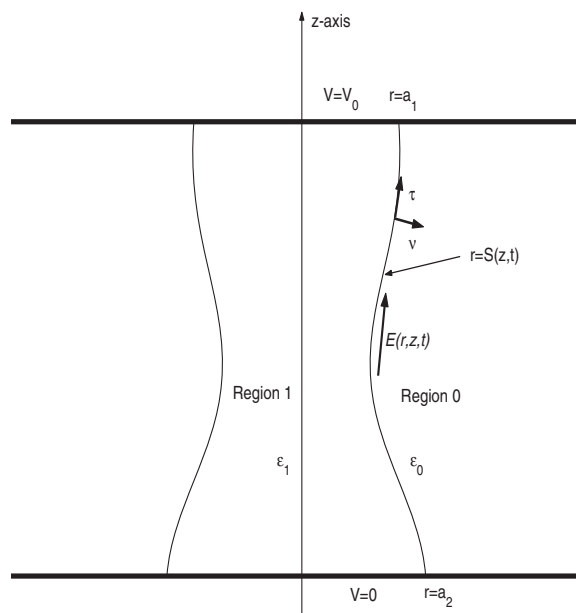


FIG. 1. A cross section of the liquid bridge showing the geometry of the problem.

by V_0 . These scalings are the capillary scales appropriate in Rayleigh instabilities of inviscid liquid jets and bridges (see Drazin and Reid (1981, Chapter 1)). The dimensionless free surface is given by $r = S(z, t)$ in a cylindrical coordinate system. Using a cylindrical coordinate system (r, θ, z) with the lower electrode at $z = 0$, the governing equations in region 1 are

$$(2.1) \quad \mathbf{u}_t + \mathbf{u} \cdot \nabla \mathbf{u} = -\nabla p - B \mathbf{e}_z,$$

$$(2.2) \quad \nabla \cdot \mathbf{u} = 0, \quad 0 \leq r < S(z, t), \quad 0 < z < \frac{1}{2},$$

where \mathbf{e}_z is the unit vector along the z -axis. The parameter $B = \frac{\rho g L R}{\sigma}$, where g is the acceleration due to gravity, is the Bond number defined as the ratio of gravitational to surface tension forces—when $B = 0$ gravity is absent. The curl-free electric field is described in terms of a voltage potential by $\mathbf{E} = -\nabla V$ in each appropriate region, which is the relevant electrostatic formulation (see, for example, Jackson (1962, Chapters 1–3)). It follows that the voltage potentials satisfy the Laplace equations

$$(2.3) \quad \Delta V = 0, \quad 0 \leq r < S(z, t), \quad 0 < z < \frac{1}{2},$$

$$(2.4) \quad \Delta V^0 = 0, \quad S(z, t) < r < \infty, \quad 0 < z < \frac{1}{2},$$

where Δ is the Laplacian in cylindrical coordinates. The boundary conditions at the electrodes are

$$(2.5) \quad V(r, 0, t) = V^0(r, 0, t) = 0,$$

$$(2.6) \quad V\left(r, \frac{1}{2}, t\right) = V^0\left(r, \frac{1}{2}, t\right) = 1.$$

In addition, the electric field far from the liquid bridge is uniform, that is,

$$(2.7) \quad \lim_{r \rightarrow \infty} V^0 = 2z.$$

The flow is irrotational, and hence we can write $\mathbf{u} = \nabla\Phi$, with $\Phi(r, z, t)$ to be determined. The continuity equation (2.2) implies that Φ is a harmonic function,

$$(2.8) \quad \Delta\Phi = 0, \quad 0 \leq r < S(z, t), \quad 0 < z < \frac{1}{2},$$

with no penetration boundary conditions at the plates

$$(2.9) \quad \Phi_z(r, 0, t) = 0, \quad 0 \leq r \leq a_1,$$

$$(2.10) \quad \Phi_z\left(r, \frac{1}{2}, t\right) = 0, \quad 0 \leq r \leq a_2,$$

where a_1 and a_2 are the dimensionless radial locations of the fixed contact rings the liquid bridge makes with the lower and upper electrodes, respectively, and are taken to be different. If Φ is known, the momentum equations (2.1) determine the pressure at any point in the fluid.

On the moving interface $r = S(z, t)$ the electric potential satisfies a continuity condition,

$$(2.11) \quad [V]_1^0 = 0,$$

and a no flux condition (i.e., continuity of the normal component of the displacement field $\varepsilon\mathbf{E}$), which in dimensionless form is given by

$$(2.12) \quad \left[\frac{\varepsilon}{\varepsilon_0} \nabla V \cdot \nu\right]_1^0 = 0,$$

where variables inside and outside the free surface take subscripts or superscripts 1 and 0, respectively, and ν is the exterior unit normal vector to S . For the fluid dynamics we write the boundary conditions at the interface in terms of the stress tensor T_{ij} whose dimensional form is

$$(2.13) \quad T_{ij} = -p\delta_{i,j} + \varepsilon \left(E_i E_j - \frac{1}{2} |E|^2 \delta_{i,j} \right),$$

where E_i is the i th component of the electric field \mathbf{E} in an orthonormal basis. In the presence of surface tension the dimensional normal stress balance reads

$$(2.14) \quad [\nu \cdot T \cdot \nu]_1^0 = \sigma \left(\frac{1}{R_1} + \frac{1}{R_2} \right),$$

where the notation $[\cdot]_1^0$ signifies that we subtract values of the quantity in square brackets in region 1 from corresponding values in region 0, e.g., $V^0 - V$; the quantity $(\frac{1}{R_1} + \frac{1}{R_2})$ is the sum of the principal radii of curvature on S . The Bernoulli boundary condition on $r = S(z, t)$ is derived by integration of Euler's equations (2.1) and elimination of the pressure jump across the interface given by the normal stress condition (2.13). Performing the calculation and making the equation dimensionless using the scalings introduced earlier yields

$$(2.15) \quad \frac{D\Phi}{Dt} - \frac{1}{2} |\nabla\Phi|^2 + \left(\frac{1}{R_1} + \frac{1}{R_2} \right) + E_b \left[\frac{1}{2} \frac{\varepsilon}{\varepsilon_0} (E_\tau^2 - E_\nu^2) \right]_1^0 + Bz = 0,$$

where $\frac{D}{Dt} = \frac{\partial}{\partial t} + \nabla\Phi \cdot \nabla$ is the material derivative, τ is the unit tangent vector to S , and E_τ, E_ν are the tangential and normal components of the electric field. The parameter $E_b = \frac{\varepsilon_0 V_0^2 R}{\sigma L}$ is an electric Weber number measuring the ratio of electrical to capillary stresses (see Tilley, Petropoulos, and Papageorgiou (2001) and Papageorgiou and Vanden-Broeck (2004)). Finally, we have the kinematic condition,

$$(2.16) \quad \frac{D}{Dt}(r - S) = 0.$$

In the remainder of the paper we denote the ratio of permittivities by

$$(2.17) \quad \varepsilon_p = \frac{\varepsilon_1}{\varepsilon_0}.$$

In this paper we consider the construction of equilibrium shapes (if they exist) for different physical parameters in order to assess the ability of the electric field to stabilize capillary instability and prevent collapse. We do not consider the related dynamic problem where the fluid potential Φ must also be calculated. At equilibrium, the pressure p_1 can be written as $p_1 = -\rho g z + \text{const.}$, where the first term is the hydrostatic part. The normal stress condition (2.14) provides an expression for the jump $p_1 - p_0$ at the interface (see Landau and Lifshitz (1987, Chapter 6)). Eliminating this jump using the above decomposition for p_1 and nondimensionalizing yields the following electrically modified Young–Laplace equation,

$$(2.18) \quad \left(\frac{1}{R_1} + \frac{1}{R_2} \right) + E_b \left[\frac{1}{2} \frac{\varepsilon}{\varepsilon_0} (E_\tau^2 - E_\nu^2) \right]_1^0 + Bz - \alpha = 0,$$

where the constant pressure jump term α must be found as part of the solution in order to satisfy mass conservation.

For future reference we recall the expression of the sum of the principal radii of curvature for axisymmetric surfaces,

$$(2.19) \quad \left(\frac{1}{R_1} + \frac{1}{R_2} \right) = \frac{1}{S(1 + S'^2)^{\frac{1}{2}}} - \frac{S''}{(1 + S'^2)^{\frac{3}{2}}},$$

where primes denote z -derivatives. The solution of this problem constitutes a non-linear problem which must be addressed numerically. We emphasize that equilibrium states may not exist for arbitrary fixed values of bridge radii a_1 and a_2 at the electrodes; see boundary condition (2.10); in the case of a perfectly cylindrical bridge, $S(z, t) = a_1 = a_2$, it is well known that if $a_1 < \frac{1}{2\pi}$ and no electric field acts, the bridge is unstable and undergoes a topological transition to ultimately form two drops, one attached to the lower electrode and the other to the upper electrode.

3. The electric field problem. In order to determine the equilibrium positions or the dynamic evolution of the liquid bridge, we need to be able to compute very accurately and efficiently the electric potential V for a given shape S . The quantities of interest in our problem are the tangential and the normal derivatives of V on S .

3.1. Formulation of the integral equation for $\frac{\partial V}{\partial \nu}|_1$. Let $G(x, y, z, x_0, y_0, z_0)$ be the Green's function defined in the region $0 \leq z \leq \frac{1}{2}$, $0 \leq z_0 \leq \frac{1}{2}$ satisfying

$$\begin{aligned} \Delta_{x,y,z} G &= -\delta_{x_0, y_0, z_0}, \\ G(x, y, 0, x_0, y_0, z_0) &= 0, \end{aligned}$$

$$G\left(x, y, \frac{1}{2}, x_0, y_0, z_0\right) = 0,$$

$$\lim_{r \rightarrow \infty} \left(G - \frac{1}{2\pi} \log \frac{1}{r}\right) = 0.$$

Using this Dirichlet Green's function and (2.3) and applying Green's theorem, we obtain, for points (x_0, y_0, z_0) in region 1,

$$(3.1) \quad (V - 2z_0) = - \int_S \frac{\partial G}{\partial \nu_{x,y,z}} (V - 2z) ds(x, y, z) + \int_S G \frac{\partial(V - 2z)}{\partial \nu_{x,y,z}} \Big|_1 ds(x, y, z).$$

For points in region 0, using the asymptotic behavior of G at infinity given above and the fact that $(V - 2z)$ approaches 0 at infinity, we obtain

$$(3.2) \quad (V - 2z_0) = \int_S \frac{\partial G}{\partial \nu_{x,y,z}} (V - 2z) ds(x, y, z) - \int_S G \frac{\partial(V - 2z)}{\partial \nu_{x,y,z}} \Big|_0 ds(x, y, z).$$

Next, we take the limit of the normal derivative of (3.1) and add it to the limit as (x_0, y_0, z_0) approaches S of the normal derivative of (3.2); using standard properties of single and double layer potentials, we obtain the integral equation for $\frac{\partial V}{\partial \nu} \Big|_1$

$$(3.3) \quad \frac{1}{2}(1 + \varepsilon_p) \frac{\partial V}{\partial \nu} \Big|_1 - (1 - \varepsilon_p) \int_S \frac{\partial G}{\partial \nu_{x_0, y_0, z_0}} \frac{\partial V}{\partial \nu} \Big|_1(x, y, z) ds(x, y, z) = 2\nu \cdot e_z.$$

After solving (3.3), we can find the potential V using the following formula, which is obtained by taking the limit of (3.1) as (x_0, y_0, z_0) approaches S and adding it to the corresponding limit of (3.2):

$$(3.4) \quad V = 2z_0 + (1 - \varepsilon_p) \int_S G \frac{\partial V}{\partial \nu} \Big|_1(x, y, z) ds(x, y, z).$$

The domain of integration for (3.3) can be greatly simplified by taking advantage of axisymmetry. We can integrate separately in the variable θ , the polar angle in cylindrical coordinates, since $\frac{\partial V}{\partial \nu} \Big|_1(x, y, z)$ is independent of θ ; this yields

$$(3.5) \quad \frac{1}{2}(1 + \varepsilon_p) \frac{\partial V}{\partial \nu} \Big|_1 - (1 - \varepsilon_p) \int_S \left(\int_0^{2\pi} \frac{\partial G}{\partial \nu_{x_0, y_0, z_0}} d\theta \right) \frac{\partial V}{\partial \nu} \Big|_1(r, z) ds(r, z) = 2\nu \cdot e_z.$$

The above equation is an integral equation along the curve defined by the cross section of S by any plane containing the z -axis. In order to simplify notation, we also denote by S that curve in the r, z coordinates. The integral equation (3.5) now involves a new Green's function

$$(3.6) \quad H(r, z, r_0, z_0) = \int_0^{2\pi} G d\theta$$

or, more precisely, the normal derivative of H . Integral equation (3.5) thus becomes

$$(3.7) \quad \frac{1}{2}(1 + \varepsilon_p) \frac{\partial V}{\partial \nu} \Big|_1 - (1 - \varepsilon_p) \int_S \frac{\partial H}{\partial \nu_{r_0, z_0}} \frac{\partial V}{\partial \nu} \Big|_1(r, z) ds(r, z) = 2\nu \cdot e_z.$$

We describe next the procedure to obtain G used in (3.6).

3.2. Ewald’s method for evaluating the Green’s function G . Ewald’s method refers to the technique for rapidly convergent summations of series representations of Green’s functions, first uncovered by Ewald in his original paper (see Ewald (1921)). It has been applied in different areas of mathematical physics, as, for example, in the dynamic theory of crystal lattices (see Born and Huang (1954)). Linton (1998, 1999) has shown how Ewald’s method can be successfully applied in electromagnetic applications.

In our case, the Green’s function G will be obtained from the periodic Green’s function $P(x, y, z, x_0, y_0, z_0)$ that satisfies

$$\begin{aligned} \Delta_{x,y,z}P &= \sum_{n=-\infty}^{n=\infty} -\delta_{x_0,y_0,z_0+n}, \\ P(x, y, z + 1, x_0, y_0, z_0) &= P(x, y, z, x_0, y_0, z_0), \\ \lim_{r \rightarrow \infty} \left(P - \frac{1}{2\pi} \log \frac{1}{r} \right) &= 0. \end{aligned}$$

The most straightforward way of expressing the Green’s function P is through the formal series

$$(3.8) \quad P(x, y, z, x_0, y_0, z_0) = \sum_{n=-\infty}^{n=\infty} G_0(x - x_0, y - y_0, z - z_0 - n),$$

where G_0 is the free-space Green’s function defined by

$$(3.9) \quad G_0(x, y, z, x_0, y_0, z_0) = \frac{1}{4\pi|(x - x_0, y - y_0, z - z_0)|}.$$

A natural idea for studying the integral equation (3.5) is to decompose H as $H = H_0 + (H - H_0)$. The singular part of H is the integrated free-space Green’s function and has been well documented. The $(H - H_0)$ part is smooth. This decomposition enables us to maintain accuracy in a consistent manner. Starting from the free-space Green’s function it is well known that integration in the angle θ yields

$$(3.10) \quad H_0(r, z, r_0, z_0) = \frac{1}{\pi} \frac{1}{\sqrt{(r + r_0)^2 + (z - z_0)^2}} K(m),$$

where $m = \frac{4rr_0}{(r+r_0)^2+(z-z_0)^2}$, and K is the complete elliptic integral function defined by

$$(3.11) \quad K(m) = \int_0^{\frac{\pi}{2}} \frac{d\theta}{(1 - m \sin^2 \theta)^{\frac{1}{2}}}.$$

From standard properties of elliptic functions (see Abramowitz and Stegun (1992), for example) we know that $K(m) \sim -\frac{1}{2} \log(1 - m)$ as m approaches 1. We now describe our approach for the evaluation of the complete elliptic function K appearing in the evaluation of H_0 . It is well known that the elliptic function $K(m)$ can be written as

$$K(m) = K1(m) + \log(1 - m)K2(m),$$

for $0 \leq m < 1$, where $K1$ and $K2$ are two smooth functions which can be efficiently approximated by polynomials for $0 \leq m < 1$. More precisely, we will use the approximation

$$K(m) \simeq PK1(m) + \log(1 - m)PK2(m),$$

where $PK1$ and $PK2$ are two polynomials. Abramowitz and Stegun (1992) provide two polynomials of degree 4 for $PK1$ and $PK2$, respectively, yielding a single precision approximation (8-digit accuracy). We were able to obtain a double precision approximation (16-digit accuracy) by solving a minimization problem in quadruple precision (32-digit accuracy). However, we had to set the degree of $PK1$ and $PK2$ to be 8.

The derivative of K can be expressed in terms of the complete elliptic integral function E :

$$K'(m) = \frac{1}{2m} \left(\frac{E(m)}{1-m} - K(m) \right),$$

$$\text{where } E(m) = \int_0^{\frac{\pi}{2}} (1 - m \sin^2 \theta)^{\frac{1}{2}} d\theta.$$

The singularity in $E(m)$ can be factored out as follows:

$$E(m) = E1(m) + \log(1-m)E2(m),$$

where $E1$ and $E2$ are smooth. $E(m)$ is in turn approximated by polynomials:

$$E(m) \simeq PE1(m) + \log(1-m)PE2(m).$$

Here, too, we obtained a double precision approximation by solving a minimization problem in quadruple precision. We had to set the degree of $PE1$ and $PE2$ to be 8.

3.2.1. Evaluation of the periodic Green's function. The formal sum (3.8) is not convergent and as such cannot be used in the construction of G . If instead we sum the x -, y -, or z -derivative of each term, we obtain a sum that converges very slowly. The series appearing in the following calculation are formal, although taking one derivative in any of the variables will make them locally uniformly convergent. To ease notation, P will temporarily designate $P(x, y, z, 0, 0, 0)$.

The basis of Ewald's method is to rewrite expression (3.8) in terms of the following integral representation:

$$P = \frac{1}{4\pi} \sum_{n=-\infty}^{n=\infty} \frac{2}{\sqrt{\pi}} \int_0^{\infty} e^{-((z-n)^2+x^2+y^2)\rho^2} d\rho$$

$$= \frac{1}{4\pi} \left\{ \sum_{n=-\infty}^{n=\infty} \frac{2}{\sqrt{\pi}} \int_0^1 e^{-((z-n)^2+x^2+y^2)\rho^2} d\rho + \sum_{n=-\infty}^{n=\infty} \frac{2}{\sqrt{\pi}} \int_1^{\infty} e^{-((z-n)^2+x^2+y^2)\rho^2} d\rho \right\}.$$

The last series in the above expression is rapidly convergent. Indeed, for $0 \leq z \leq 1$ and $|n| \geq 2$,

$$\frac{2}{\sqrt{\pi}} \int_1^{\infty} e^{-((z-n)^2+x^2+y^2)\rho^2} d\rho \leq C e^{-(1-|n|)^2},$$

for some constant C , independent of x , y , z , and n . Note that it is crucial that the lower bound be different from 0 in the above integral for the estimate to hold. A similar estimate for the same integrand does not hold when integrating on the interval $[0, 1]$. Thus we apply a transformation to the series $\sum_{n=-\infty}^{n=\infty} \frac{2}{\sqrt{\pi}} \int_0^1 e^{-((z-n)^2+x^2+y^2)\rho^2} d\rho$. Denoting

$$(3.12) \quad h(x, y, z) = \sum_{n=-\infty}^{n=\infty} e^{-((z-n)^2+x^2+y^2)\rho^2}$$

and noting that h is a periodic function in z of period 1, we can calculate its Fourier coefficient $\hat{h}(l)$,

$$\begin{aligned} \hat{h}(l) &= \int_0^1 \sum_{n=-\infty}^{n=\infty} e^{-((z-n)^2+x^2+y^2)\rho^2-2i\pi lz} dz \\ &= \int_{-\infty}^{\infty} e^{-(z^2+x^2+y^2)\rho^2-2i\pi lz} dz \\ &= e^{-\frac{l^2\pi^2}{\rho^2}-(x^2+y^2)\rho^2} \frac{\sqrt{\pi}}{\rho}. \end{aligned}$$

Hence

$$(3.13) \quad h(x, y, z) = \sum_{n=-\infty}^{n=\infty} e^{-\frac{n^2\pi^2}{\rho^2}-(x^2+y^2)\rho^2+2i\pi nz} \frac{\sqrt{\pi}}{\rho}.$$

Finally, substituting (3.13) into (3.12) we find that

$$(3.14) \quad \begin{aligned} P &= \frac{1}{4\pi} \left\{ \sum_{n=-\infty}^{n=\infty} \frac{2}{\sqrt{\pi}} \int_0^1 e^{-\frac{n^2\pi^2}{\rho^2}-(x^2+y^2)\rho^2+2i\pi nz} \frac{\sqrt{\pi}}{\rho} d\rho \right. \\ &\quad \left. + \sum_{n=-\infty}^{n=\infty} \frac{2}{\sqrt{\pi}} \int_1^{\infty} e^{-((z-n)^2+x^2+y^2)\rho^2} d\rho \right\}. \end{aligned}$$

Note that in this new expression for P , for $n \neq 0$, the term

$$\int_0^1 e^{-\frac{n^2\pi^2}{\rho^2}-(x^2+y^2)\rho^2+2i\pi nz} \frac{\sqrt{\pi}}{\rho} d\rho,$$

in the first series, is less than $Ce^{-n^2\pi^2}$, for some constant C , independent of x, y, z , and n . The first integral in the series expression (3.14) is not convergent for $n = 0$. However, that difficulty disappears when one derivative is taken with respect to any of the variables; alternatively we can add an integrating term which is compatible with all the derivatives and with the behavior of P as r tends to infinity. We also notice that the first sum in (3.14) can be changed into a sum of cosines. Finally, we obtain the expression (reintroducing the sources at (x_0, y_0, z_0))

$$(3.15) \quad \begin{aligned} P(x, y, z, x_0, y_0, z_0) &= \frac{1}{2\pi} \sum_{n=1}^{n=\infty} \left\{ \int_0^1 2 \cos(2\pi n(z - z_0)) e^{-\frac{n^2\pi^2}{\rho^2}-((x-x_0)^2+(y-y_0)^2)\rho^2} \frac{d\rho}{\rho} \right\} \\ &\quad + \frac{1}{2\pi} \int_0^1 \frac{e^{-((x-x_0)^2+(y-y_0)^2)\rho^2} - 1}{\rho} d\rho \\ &\quad + \frac{1}{2\pi} \sum_{n=-\infty}^{n=\infty} \frac{1}{\sqrt{\pi}} \int_1^{\infty} e^{-(z-z_0-n)^2\rho^2} e^{-((x-x_0)^2+(y-y_0)^2)\rho^2} d\rho. \end{aligned}$$

Next, we briefly demonstrate the stated asymptotic behavior of (3.15) as r approaches infinity. It is clear that the series terms in the first and the last terms of (3.15) all tend uniformly to zero as r approaches infinity. We then take the r -derivative of the second term to obtain

$$(3.16) \quad \frac{1}{2\pi} \int_0^1 -\rho(2r - 2r_0 \cos(\theta - \theta_0)) e^{-(r^2+r_0^2-2rr_0 \cos(\theta-\theta_0))\rho^2} d\rho,$$

which can be integrated exactly. From there we see that the principal part of (3.15) as r grows large is $-\frac{1}{2\pi r}$, as expected.

3.2.2. The axisymmetric form of the periodic Green’s function. The expression (3.15) for the 1-periodic Green’s function can be specialized further to an expression which is useful for the axisymmetric problems of interest here. This is achieved by integrating P in the angle θ between 0 and 2π , which yields the following novel expression for the axisymmetric Green’s function Q , say,

$$\begin{aligned}
 (3.17) \quad Q(r, z, r_0, z_0) = & \sum_{n=1}^{n=\infty} \left\{ \int_0^1 2 \cos(2\pi n(z - z_0)) e^{-\frac{n^2 \pi^2}{\rho^2} - (r-r_0)^2 \rho^2} I_0(2rr_0 \rho^2) e^{-2rr_0 \rho^2} \frac{d\rho}{\rho} \right\} \\
 & + \int_0^1 \frac{e^{-(r-r_0)^2 \rho^2} I_0(2rr_0 \rho^2) e^{-2rr_0 \rho^2} - 1}{\rho} d\rho \\
 & + \sum_{n=-\infty}^{n=\infty} \left\{ \frac{1}{\sqrt{\pi}} \int_1^\infty e^{-(z-z_0-n)^2 \rho^2} e^{-(r-r_0)^2 \rho^2} I_0(2rr_0 \rho^2) e^{-2rr_0 \rho^2} d\rho \right\}.
 \end{aligned}$$

This formula is new as far as we know. I_0 denoted the modified Bessel function of the first kind. Note that $I_0(s)e^{-s}$ is a bounded function of $s > 0$ and is sometimes referred to as the rescaled modified Bessel function of the first kind. Derivatives of H can be obtained by differentiating each term in the series from expression (3.17). For faster computations, it is worth keeping in mind that Q satisfies the following identities:

$$\begin{aligned}
 Q(r, z, r_0, z_0) &= Q(r, z - z_0, r_0, 0), \\
 Q(r, z, r_0, 0) &= Q(r, -z, r_0, 0), \\
 Q(r, z, r_0, z_0) &= Q(r_0, z, r, z_0).
 \end{aligned}$$

Finally, we obtained the following formula for $Q - H_0$ (H_0 is the free-space Green’s function; see (3.10)), valid for points where $(r, z) = (r_0, z_0)$, in the range $0 \leq z \leq \frac{1}{2}$. Since

$$\begin{aligned}
 H_0(r, z, r_0, z_0) &= \frac{1}{4\pi} \int_0^{2\pi} \frac{d\theta}{\sqrt{(z - z_0)^2 + r^2 + r_0^2 - 2rr_0 \cos \theta}} \\
 &= \frac{1}{4\pi} \int_0^{2\pi} \int_0^\infty \frac{2}{\sqrt{\pi}} e^{-((z-z_0)^2 + r^2 + r_0^2 - 2rr_0 \cos \theta) \rho^2} d\rho d\theta \\
 &= \frac{1}{\sqrt{\pi}} \int_0^\infty e^{-((z-z_0)^2 + (r-r_0)^2) \rho^2} I_0(2rr_0 \rho^2) e^{-2rr_0 \rho^2} d\rho,
 \end{aligned}$$

we infer, upon subtraction, that

$$\begin{aligned}
 (3.18) \quad (Q - H_0)(r, z, r, z) = & \sum_{n=1}^{n=\infty} \int_0^1 2e^{-\frac{n^2 \pi^2}{\rho^2}} I_0(2r^2 \rho^2) e^{-2r^2 \rho^2} \frac{d\rho}{\rho} \\
 & + \int_0^1 \frac{I_0(2r^2 \rho^2) e^{-2r^2 \rho^2} - 1}{\rho} d\rho - \frac{1}{\sqrt{\pi}} \int_0^1 I_0(2r^2 \rho^2) e^{-2r^2 \rho^2} d\rho \\
 & + \sum_{n=-\infty, n \neq 0}^{n=\infty} \frac{1}{\sqrt{\pi}} \int_1^\infty e^{-n^2 \rho^2} I_0(2r^2 \rho^2) e^{-2r^2 \rho^2} d\rho.
 \end{aligned}$$

Formula (3.18) is particularly interesting since each of the functions Q and H_0 is singular at points where $(r, z) = (r_0, z_0)$, but the difference can be calculated explicitly as given above.

3.2.3. Final calculation of the Green's function G . The function Q is the 1-periodic axisymmetric Green's function which would be pertinent to axially periodic flows such as infinitely long liquid jets, for example. The liquid bridge problem, however, is of finite extent a Dirichlet axisymmetric Green's function (we called this G) and is appropriate. It is simple to obtain G from Q by using periodicity, and the following formula is obtained:

$$(3.19) \quad G(r, z, r_0, z_0) = Q(r, z - z_0, r_0, 0) - Q(r, -z - z_0, r_0, 0).$$

Note that $Q(r, -z - z_0, r_0, 0)$ is not singular if $z \neq z_0$ and $0 \leq z, z_0 \leq \frac{1}{2}$ are simultaneously satisfied. As indicated earlier, we chose to have the function H_0 bear the singularity. In effect, we used the following decomposition:

$$(3.20) \quad G(r, z, r_0, z_0) = H_0(r, z, r_0, z_0) + (Q - H_0)(r, z, r_0, z_0) - Q(r, -z - z_0, r_0, 0).$$

4. Algorithm and numerical tests of the Green's function calculation.

In this section we undertake numerical tests for the evaluation of H_0 and Q and their derivatives. All other functions relevant to our problem can then be obtained in a straightforward way as explained above.

4.1. Evaluating the axisymmetric and periodic Green's function Q .

In this section we describe our algorithm for evaluating Q with a 10-digit accuracy throughout. (It is understood that more nodes should be used if higher accuracy is desired and fewer nodes if faster speed is desired, sacrificing some of the accuracy.) Analogous algorithms for evaluating $\frac{\partial Q}{\partial r}$ and $\frac{\partial Q}{\partial z}$ were also constructed, but we omit their detailed description since the steps are completely equivalent.

We first estimate the general terms in the infinite series expression (3.17) for Q by

$$\left| \int_0^1 2 \cos(2\pi n(z - z_0)) e^{-\frac{n^2 \pi^2}{\rho^2} - (r-r_0)^2 \rho^2} I_0(2rr_0 \rho^2) e^{-2rr_0 \rho^2} \frac{d\rho}{\rho} \right| \leq C e^{-n^2 \pi^2},$$

$$\left| \int_1^\infty e^{-(z-z_0-n)^2 \rho^2} e^{-(r-r_0)^2 \rho^2} I_0(2rr_0 \rho^2) e^{-2rr_0 \rho^2} d\rho \right| \leq C e^{-(|n|-\frac{1}{2})^2},$$

where C is a constant independent of r , z , r_0 , and z_0 , provided that $0 \leq z, z_0 \leq \frac{1}{2}$. This explains why it is sufficient to truncate the first series in (3.17) at $n = 2$ and to run a summation for the second series between $n = -5$ and $n = 5$, since C is reasonably small and our accuracy goal of 10 digits is met; see the results below.

We now explain the numerical procedure for evaluating the integrals involved in the series (3.17) while maintaining the set 10-digit accuracy. For the integrals

$$\int_0^1 2 \cos(2\pi n(z - z_0)) e^{-\frac{n^2 \pi^2}{\rho^2} - (r-r_0)^2 \rho^2} I_0(2rr_0 \rho^2) e^{-2rr_0 \rho^2} \frac{d\rho}{\rho},$$

$$\int_0^1 \frac{e^{-(r-r_0)^2 \rho^2} I_0(2rr_0 \rho^2) e^{-2rr_0 \rho^2} - 1}{\rho} d\rho,$$

we make a linear change of variables to transform the range of integration onto $[-1, 1]$ and apply a 64-point Legendre quadrature. Nodes and weights can be computed by a service routine from NETLIB, for example.

The integrals involved in the last term in (3.17) require slightly more care. Since these integrals depend on z and z_0 only through $z - z_0$, we temporarily set $z_0 = 0$ to

ease notation. Set $L = (z - n)^2 + (r - r_0)^2$. Substitutions lead to the identity

$$(4.1) \quad \int_1^\infty e^{-(z-n)^2\rho^2} e^{-(r-r_0)^2\rho^2} I_0(2rr_0\rho^2) e^{-2rr_0\rho^2} d\rho \\ = \frac{e^{-L}}{2\sqrt{L}} \int_0^\infty e^{-s} I_0\left(2rr_0\left(\frac{s}{L} + 1\right)\right) e^{-2rr_0\left(\frac{s}{L} + 1\right)} (s + L)^{-\frac{1}{2}} ds.$$

The integral (4.1) is denoted by I_L . If $L \geq 1$, a Laguerre quadrature in s is applied to the integral in (4.1). We picked a 64-point scheme, but only the first 24 nodes needed to be considered. For small L , the values of the integrand become more and more important for an accurate numerical value of I_L . We first present an algorithm based on splitting the interval of integration for I_L . If $.1 \leq L < 1$, the domain of integration for I_L is split into two parts, the first part being $[0, 1]$ and the second $[1, \infty)$. After a linear change of variables, we applied Legendre and Laguerre quadratures to the two parts, respectively. For $.01 \leq L < .1$, we split the domain of integration for I_L into three parts, the first part being $[0, 10L]$, the second $[10L, 1]$, and the third $[1, \infty)$. Applying a linear change of variables, the two intervals $[10L, 1]$ and $[1, \infty)$ are transformed into $[-1, 1]$ and $[0, \infty)$, respectively. Legendre and Laguerre quadratures are then applied. The same idea is iterated to each case where $10^{-(p+1)} \leq L < 10^{-p}$, where p is a positive integer. As p grows, it is crucial to use more and more points near 0 for maximum accuracy. Note that a small value for L can at most occur for a single value of n in the series (3.17). In addition, we did not need to use values for L smaller than 10^{-4} for the problem considered here.

Alternatively, if $z - z_0$ is smaller than, say, .25, we may use the decomposition $Q = (Q - H_0) + H_0$, where the formula for $(Q - H_0)$ is

$$(Q - H_0)(r, z, r_0, z_0) \\ = \sum_{n=1}^{n=\infty} \left\{ \int_0^1 2 \cos(2\pi n(z - z_0)) e^{-\frac{n^2\pi^2}{\rho^2} - (r-r_0)^2\rho^2} I_0(2rr_0\rho^2) e^{-2rr_0\rho^2} \frac{d\rho}{\rho} \right\} \\ + \int_0^1 \frac{e^{-(r-r_0)^2\rho^2} I_0(2rr_0\rho^2) e^{-2rr_0\rho^2} - 1}{\rho} d\rho \\ - \frac{1}{\sqrt{\pi}} \int_0^1 e^{-((z-z_0)^2 + (r-r_0)^2)\rho^2} I_0(2rr_0\rho^2) e^{-2rr_0\rho^2} d\rho \\ + \sum_{n=-\infty, n \neq 0}^{n=\infty} \left\{ \frac{1}{\sqrt{\pi}} \int_1^\infty e^{-(z-z_0-n)^2\rho^2} e^{-(r-r_0)^2\rho^2} I_0(2rr_0\rho^2) e^{-2rr_0\rho^2} d\rho \right\}.$$

That way, all the integrals I_L can be evaluated in a single step by Laguerre quadrature. This is the approach that we choose to follow throughout the rest of the paper.

Derivatives of Q are obtained by differentiating analytically the formula for Q . Subsequently, numerical evaluations of derivatives of Q are performed analogously to numerical evaluations of Q .

4.2. Algorithm verification.

4.2.1. Comparison with the obvious approach. In this section we evaluate the accuracy of our summation method by considering a specific numerical example. We pick the following numerical values,

$$r = .24, \quad z = .11, \quad r_0 = .25, \quad z_0 = 0,$$

and we seek to evaluate $\frac{\partial Q}{\partial z}(r, z, r_0, z_0)$.

TABLE 1
Evaluation of $\frac{\partial Q}{\partial z}$ using formulas (4.2) and (4.3).

N	Numerical value for (4.3)
32	-5.84598547910539
64	-5.84595180542009
128	-5.84595180539143

In order to obtain an independent check, we first use the straightforward formula (3.8). Rewriting (3.8) in terms of cylindrical coordinates and taking the z -derivative, we obtain

$$(4.2) \quad \frac{\partial P}{\partial z}(r, \theta, z, r_0, \theta_0, z_0) = \sum_{n=-\infty}^{n=\infty} \frac{n - z}{4\pi(r^2 + r_0^2 + (z - n)^2 - 2rr_0 \cos(\theta - \theta_0))^{\frac{3}{2}}}.$$

Note that the infinite sum in (4.2) is convergent. It can be evaluated to any desired precision with the help of software such as Mathematica. To obtain an approximation for the axisymmetric periodic Green's function, $\frac{\partial Q}{\partial z}(r, z, r_0, z_0)$, we need to integrate (4.2) with respect to θ . Due to periodicity in θ , this is achieved with spectral accuracy by a trapezium rule, and we can therefore approximate $\frac{\partial Q}{\partial z}(r, z, r_0, z_0)$ by

$$(4.3) \quad \frac{2\pi}{N} \sum_{j=1}^N \frac{\partial P}{\partial z} \left(r, \frac{2\pi j}{N}, z, r_0, 0, 0 \right)$$

for different values of N . After some painstakingly slow calculations (close to 20 minutes of CPU time), we arrive at the following numerical values.

If, instead, we sum the series using the Ewald method described above, we obtain in less than 0.002 seconds (using the same CPU) the value -5.84595180540356 . The values in Table 1 suggest that the first 12 digits are correct.

In a second example, we consider the point,

$$r = .24, \quad z = 0, \quad r_0 = .25, \quad z_0 = 0,$$

and seek to evaluate numerically $\frac{\partial Q}{\partial r}(r, z, r_0, z_0)$. Note that, in this second case, we are much closer to a singularity. In order to obtain an independent check, we first use the straightforward formula (3.8). Switching to cylindrical coordinates in (3.8) and taking the r -derivative, we obtain

$$(4.4) \quad \frac{\partial P}{\partial r}(r, \theta, z, r_0, \theta_0, z_0) = \sum_{n=-\infty}^{n=\infty} \frac{-2(r - r_0 \cos(\theta - \theta_0))}{4\pi(r^2 + r_0^2 + (z - n)^2 - 2rr_0 \cos(\theta - \theta_0))^{\frac{3}{2}}}.$$

The infinite sum in (4.4) is convergent and can be evaluated to any desired precision with the help of software such as Mathematica, for example. As in the previous example, we can approximate $\frac{\partial Q}{\partial r}(r, z, r_0, z_0)$ by

$$(4.5) \quad \frac{2\pi}{N} \sum_{j=1}^N \frac{\partial P}{\partial r} \left(r, \frac{2\pi j}{N}, z, r_0, 0, 0 \right)$$

for different values of N . This time, the naive algorithm is even slower, taking well over one hour on the same CPU as above to complete. The calculated values for different N are given in Table 2.

TABLE 2
Evaluation of $\frac{\partial Q}{\partial z}$ at a point closer than previously to a singularity.

N	Numerical value for (4.5)
64	83.51214241091419
128	61.19439435982529
256	59.01913795859809
512	59.00307731552657
1024	59.00307666864498

The corresponding value using Ewald summations is obtained in less than 0.002 seconds of CPU time and is equal to 59.0030766686615, again showing 12-digit accuracy. The function Q itself was also obtained by numerical integration of either of our computed values for $\frac{\partial Q}{\partial r}$ or $\frac{\partial Q}{\partial z}$; our approximation of Q , then, is correct up to a constant. Finally, an asymptotic expansion of the middle term in (3.17) shows that Q exhibits the correct behavior as r becomes large.

4.2.2. Accuracy and efficiency of derivatives of the Green's function.

The reader probably feels that the comparison from the last paragraph was unfair since the integral $\int_0^{2\pi} G_0(r \cos \theta, r \sin \theta, z - n, r_0 \cos \theta_0, r_0 \sin \theta_0, z_0) d\theta$ is exactly equal to $H_0(r, z - n, r_0, z_0)$ and the z - or the r -derivative of the latter forms a convergent series. We try out this idea for the calculation of $\frac{\partial Q}{\partial z}(r, z, r_0, z_0)$ for $r = .24$, $z = .11$, $r_0 = .25$, and $z_0 = 0$, the same values as in the first example of the preceding paragraph, using the formula

$$(4.6) \quad \frac{\partial Q}{\partial z}(r, z, r_0, z_0) = \sum_{n=-\infty}^{n=\infty} \frac{\partial H_0(r, z - n, r_0, z_0)}{\partial z}.$$

In our code, each evaluation of the elliptic functions E or K was performed by using the polynomials $PE1$, $PE2$, $PK1$, and $PK2$ of degree 8 introduced earlier, which is very economical. We decide to truncate the series (4.6) when the general term becomes smaller than 10^{-12} . We find the value -5.84595180540555 , which has 12 accurate digits. The truncation value for n was 707107. The operations were performed in 0.804 seconds, that is, about 800 times as slow as when applying Ewald's method. Note that for Ewald's method, it suffices to run the first sum in formula (3.17) for n from 1 to 2 and to run the second sum for n from -5 to 5.

We now try to reproduce the second example from the last section, where $r = .24$, $z = 0$, $r_0 = .25$, and $z_0 = 0$. We evaluate

$$(4.7) \quad \frac{\partial Q}{\partial r}(r, z, r_0, z_0) = \sum_{n=-\infty}^{n=\infty} \frac{\partial H_0(r, z - n, r_0, z_0)}{\partial r}.$$

As above, we truncate the series (4.7) when the general term becomes smaller than 10^{-12} . We find the value 59.0030766687182, which has 12 accurate digits. The truncation value for n was again 707107. Notice that it was expected for the truncation number to be the same in either example because the series converges as $(z - n)^{-2}$ and $|(707107)^{-2} - (707107 - .11)^{-2}| < 10^{-12}$. The operations were performed in 0.797 seconds, again about 800 times as slow as when applying Ewald's method.

Finally, we compare performances for the evaluation of Q itself. As noted earlier, the series

$$\sum_{n=-\infty}^{n=\infty} H_0(r, z - n, r_0, z_0)$$

is not convergent. Instead, the series,

$$(4.8) \quad \sum_{n=-\infty}^{n=\infty} H_0(r, z - n, r_0, z_0) - \frac{1 - \delta_{0,n}}{2|n|},$$

is convergent and yields $Q(r, z, r_0, z_0)$ to within an unknown constant, which is sufficient for our problem. To test this formula on a numerical example, we evaluate

$$Q(.24, .1, .25, 0) - Q(.3, .1, .25, 0),$$

using Ewald’s method and, for comparison, the series (4.8) truncated when the general term becomes smaller than 10^{-10} . In the case of Ewald’s method we obtain 0.215472859717063 in less than .001 seconds. Using the series (4.8) we obtain 0.215472859719637 in 0.323 seconds for a truncation value of 223608. The two numerical values agree over the first 11 decimals.

Remark. Whereas algorithms for evaluating sums such as (4.6), (4.7), and (4.8) are straightforward to design, algorithms for the evaluation of the series (3.17) are nontrivial, since the terms are integrals to which quadrature rules are applied. It is quite possible that a finer analysis for the evaluation of these integrals will yield a more efficient algorithm than ours, which suggests further advantages for Ewald’s method regarding speed and accuracy.

5. Numerical solution of the integral equation for the normal component of the electric field. We recall that the function $H - H_0$ is smooth for all $0 < z, z_0 < \frac{1}{2}$ and $r, r_0 > 0$, and, as shown in the preceding section, we possess a fast and accurate technique to evaluate it, even at those points where $(r, z) = (r_0, z_0)$. Consequently, we rewrite (3.7) as

$$(5.1) \quad \begin{aligned} & \frac{1}{2}(1 + \varepsilon_p) \frac{\partial V}{\partial \nu} \Big|_1 - (1 - \varepsilon_p) \int_S \frac{\partial H_0}{\partial \nu_{r_0, z_0}} \frac{\partial V}{\partial \nu} \Big|_1(r, z) ds(r, z) \\ & - (1 - \varepsilon_p) \int_S \frac{\partial(H - H_0)}{\partial \nu_{r_0, z_0}} \frac{\partial V}{\partial \nu} \Big|_1(r, z) ds(r, z) = 2\nu \cdot e_z. \end{aligned}$$

We choose the following parametrization for S ,

$$z = z(t), \quad r = r(t), \quad 0 \leq t \leq 1,$$

such that $z(0) = 0, z(1) = \frac{1}{2}$, and rewrite (5.1) using this, to obtain

$$(5.2) \quad \begin{aligned} & \frac{1}{2}(1 + \varepsilon_p) \frac{\partial V}{\partial \nu} \Big|_1(r(t), z(t)) \\ & - (1 - \varepsilon_p) \int_0^1 \frac{\partial H_0}{\partial \nu_{r_0, z_0}}(r(v), z(v), r(t), z(t)) \frac{\partial V}{\partial \nu} \Big|_1(r(v), z(v)) r(v) \sqrt{r'(v)^2 + z'(v)^2} dv \\ & - (1 - \varepsilon_p) \int_0^1 \frac{\partial(H - H_0)}{\partial \nu_{r_0, z_0}}(r(v), z(v), r(t), z(t)) \frac{\partial V}{\partial \nu} \Big|_1(r(v), z(v)) r(v) \sqrt{r'(v)^2 + z'(v)^2} dv \\ & = 2\nu(r(t), z(t)) \cdot e_z. \end{aligned}$$

According to the properties of the elliptic function $K(m)$, the first integral in (5.2) can be expressed as

$$(5.3) \quad \int_0^1 \log |t - v| F_1(t, v) dv + \int_0^1 F_2(t, v) dv$$

for some functions F_1 and F_2 . More precisely, setting

$$m = \frac{4r(t)r(v)}{[r(t) + r(v)]^2 + [z(t) - z(v)]^2},$$

we obtain

$$\frac{\partial H_0}{\partial \nu_{r_0, z_0}}(r(v), z(v), r(t), z(t)) = \frac{1}{2\pi r(t)((r(t) + r(v))^2 + (z(t) - z(v))^2)^{\frac{1}{2}}(r'(t)^2 + z'(t)^2)^{\frac{1}{2}}} \\ \times \left[(E(m) - K(m))z'(t) + 2r(t)K(m) \frac{(r(t) - r(v))z'(t) - (z(t) - z(v))r'(t)}{(r(t) - r(v))^2 + (z(t) - z(v))^2} \right]$$

Note that $F_1(t, v)$ and $F_2(t, v)$ can be evaluated with the aid of the polynomials $PK1$, $PK2$, $PE1$, and $PE2$, introduced in the preceding section. The second integral in (5.2) can be expressed as

$$(5.4) \quad \int_0^1 F_3(t, v) dv,$$

and $F_3(t, v)$ is evaluated with the aid of the polynomials $PK1$, $PK2$, $PE1$, and $PE2$ and the rapidly converging series for H and $H - H_0$ introduced previously. We choose the collocation points $t_j = \frac{j}{n}$ for $1 \leq j \leq n - 1$. The following quadrature rules were found for each of the two types of integrals appearing in (5.3) and (5.4):

$$(5.5) \quad \int_0^1 \log |t_j - v| F(t_j, v) dv = \sum_{l=1}^{l=n-1} q_1(j, l, n) F(t_j, t_l) + O\left(\frac{\log n}{n^4}\right),$$

$$(5.6) \quad \int_0^1 F(t_j, v) dv = \sum_{l=1}^{l=n-1} q_2(l, n) F(t_j, t_l) + O\left(\frac{1}{n^4}\right).$$

The coefficients $q_1(j, l, n)$ and $q_2(l, n)$ were obtained by substituting an appropriate polynomial $P_{r,n}(v)$ interpolating $F(t_j, v)$ for v over $[\frac{r}{n}, \frac{r+1}{n}]$ followed by the following approximations:

$$(5.7) \quad \int_0^1 \log |t_j - v| F(t_j, v) dv \simeq \sum_{r=1}^{n-2} \int_{\frac{r}{n}}^{\frac{r+1}{n}} \log |t_j - v| P_{r,n}(v) dv \\ + \int_0^{\frac{1}{n}} \log |t_j - v| P_{1,n}(v) dv + \int_{\frac{n-1}{n}}^1 \log |t_j - v| P_{n-2,n}(v) dv,$$

$$(5.8) \quad \int_0^1 F(t_j, v) dv \simeq \sum_{r=1}^{n-2} \int_{\frac{r}{n}}^{\frac{r+1}{n}} P_{r,n}(v) dv + \int_0^{\frac{1}{n}} P_{1,n}(v) dv + \int_{\frac{n-1}{n}}^1 P_{n-2,n}(v) dv.$$

We proceed to obtain a system of linear equations in the unknowns $\frac{\partial V}{\partial \nu}|_1(r(t_j), z(t_j))$ for $1 \leq j \leq n - 1$. The following section is aimed at proving that this system of linear equations is well posed and yields an approximation to the true value of $\frac{\partial V}{\partial \nu}|_1(r(t_j), z(t_j))$ with the error $O(\frac{\log n}{n^4})$.

5.1. Convergence of the numerical scheme. It is possible to prove that if the integral equation (5.2) is numerically approximated as described above, then the numerical scheme converges to the unique solution of the continuous problem. We carried out our proof using elementary potential theory and the general theory of linear integral equations, referring to Kress (1999). The detailed proof appears in the appendix.

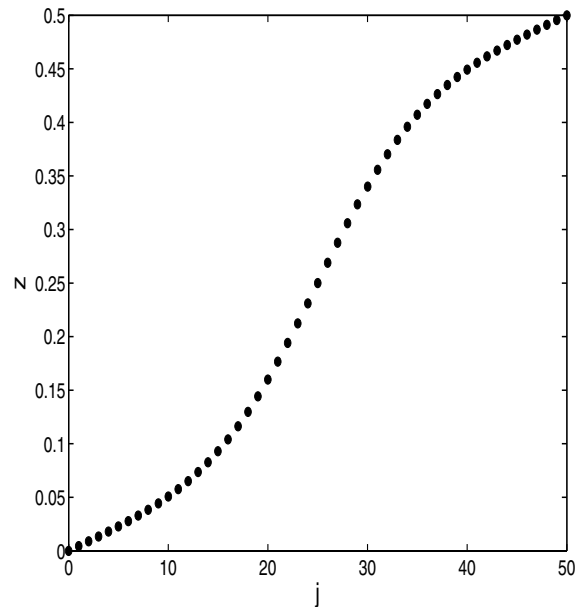


FIG. 2. The distribution of quadrature points on the z -axis for $n = 50$.

5.2. Parametrization of the interface S . In practice, the Green's function H is derived from the periodic Green's function Q through the identity

$$(5.9) \quad H(r, z, r_0, z_0) = Q(r, z - z_0, r_0, 0) - Q(r, z - z_0 - 1, r_0, 0).$$

If z_0 is close to 0 or $\frac{1}{2}$, then as (r, z) approaches (r_0, z_0) , the term $Q(r, z - z_0 - 1, r_0, 0)$ is close to being singular. An efficient numerical code must take into account that points closer to the plates are problematic. A standard method is to cluster points near the plates. To do so, we chose the following point distribution for the z variable. Set

$$g(s) = \frac{s}{1.7 - e^{-s^2}}.$$

Then pick

$$z\left(\frac{j}{n}\right) = \frac{g\left(\frac{2j}{n} - 1\right) - g(-1)}{2(g(1) - g(-1))}$$

for $0 \leq j \leq n$. In Figure 2 we plot z against j for $n = 50$.

In order to solve the integral equation (5.2) and the associated Bernoulli equation (see section 5), we need to possess accurate values for the components of the unit tangent vector and the curvature at the quadrature knots. The shape of the interface is unknown and must be determined as part of the solution. In order to obtain accurate approximations of important geometric quantities, approximate the surface S by an equation giving r as a polynomial function of z . The degree of the polynomial is fixed, and the coefficients of the polynomials are constrained. A least squares method is applied to obtain the polynomial equation at each time or iteration step. When we ran tests without the smoothing effects of the least squares method, errors in the

calculation of the curvature accumulated exponentially. The errors first appeared near the walls, because the marker points there are not allowed to move, whereas their immediate neighbors are free to move. These errors then propagated to the rest of the curve, giving it over time a ragged aspect and eventually leading to numerical overflow. We anticipate that our constrained polynomial approach is a reasonable one since we expect to find very smooth shapes at equilibrium. In addition, once a polynomial equation for the curve S is set, it is straightforward to calculate the components of the unit tangent vector and curvature.

5.3. Calculation of the potential at the interface S . As mentioned earlier, the values of V on S are calculated from $\frac{\partial V}{\partial \nu}|_1$ through the formula (3.4). In practice, we use again the decomposition $H = H_0 + (H - H_0)$; that is, we write

$$V = 2z_0 + (1 - \varepsilon_p) \int_S H_0 \frac{\partial V}{\partial \nu}|_1(r, z) ds(r, z) \\ + (1 - \varepsilon_p) \int_S (H - H_0) \frac{\partial V}{\partial \nu}|_1(r, z) ds(r, z).$$

We recall the expression for H_0 given by (3.10) and again apply the quadrature rules (5.5) and (5.6) described above. Finally, we determine $\frac{\partial V}{\partial \tau}$ from V through a fourth-order numerical differentiation scheme compatible with the accuracy of the quadratures q_1 and q_2 defined in (5.5) and (5.6). This yields the tangential derivative of V along S , which is an important quantity in our numerical solutions.

5.4. Numerical tests on a model problem. Before proceeding to numerical solutions of the electrified liquid bridge equilibria, we undertake the numerical solution of the integral equation (5.2) for a test problem with known exact solution. This provides us with a crucial test of the efficiency and accuracy of the algorithms developed here and provides a benchmark for more complex problems.

The function

$$(5.10) \quad f(r, z) = I_0(2\pi pr) \sin(2\pi pz)$$

is harmonic and equal to 0 on the two plates $z = 0$ and $z = \frac{1}{2}$ for any positive integer p . We picked the following contour for S ,

$$r = .2 - .025 \sin \left(1.8 \left(z - \frac{1}{2} \right) 2\pi \right) - \left(z - \frac{1}{2} \right),$$

for $0 \leq z \leq \frac{1}{2}$.

We start from the data $\frac{\partial f}{\partial \nu}|_S$ to solve the interior Neumann problem within S . The exact solution to this problem is $f|_S$. In order to use an integral equation very similar to (5.2), we want to solve for an unknown density μ such that

$$(5.11) \quad f = \int_S H \mu ds(r, z).$$

We take the interior limit of the normal derivative of the above identity to obtain the integral equation for μ ,

$$(5.12) \quad \frac{1}{2}\mu + \int_S \frac{\partial H}{\partial \nu_{r_0, z_0}} \mu(r, z) ds(r, z) = \frac{\partial f}{\partial \nu}.$$

TABLE 3
Relative error in solving the model problem (5.11)–(5.12).

p	n		
1	16	1.287729936141243E-003	1.714755977106271E-003
1	60	7.762965695679299E-006	1.186067134489967E-004
1	100	6.242540303816384E-006	5.431369796707948E-005
2	16	6.310690919176223E-003	3.311169996169350E-003
2	60	3.429196669294850E-005	2.448969102186786E-004
2	100	2.683594220378686E-005	1.129425510500699E-004
5	16	0.229937851009152	6.384322807134564E-002
5	60	3.224724948116380E-004	8.378366516111891E-004
5	100	1.260027832920140E-004	3.961639420588690E-004

TABLE 4
Relative error for the tangential derivative in problem (5.11)–(5.12).

p	n		
1	16	1.581671458412389E-002	5.837237070761748E-003
1	60	1.083613264814597E-004	2.295652299395658E-003
1	100	3.236637872189426E-005	1.985969562593125E-003
2	16	2.904969291019818E-002	1.199488810790314E-002
2	60	3.502947054305484E-004	4.160789204244608E-003
2	100	5.753436032240671E-005	3.567525695685254E-003
5	16	0.360893813029678	0.108292168068875
5	60	4.193195791752120E-003	8.116018733827291E-003
5	100	5.265448522853693E-004	6.785711322636750E-003

After solving (5.12) for μ , we calculate f at the quadrature nodes based on formula (5.11). Finally, we measure the relative error. In Table 3, we indicate in the third column the maximum of the relative error for $0.05 < z < 0.45$. In the fourth column, we indicate the maximum of the relative error for $0 < z < 0.05$ or for $0.45 < z < 0.5$. The first two columns contain the values of p and n , where p appears in the definition of f and measure spatial frequency, and n is the number of quadrature nodes.

In Table 4 we repeat the simulations, this time measuring the relative error in the tangential derivative of f .

6. Physical examples: Equilibrium shapes of electrified liquid bridges.

In previous sections we described how the electrified liquid bridge problem can be solved numerically using boundary integral methods. In this section we concentrate on the specific physical problem of using such methods to obtain equilibrium shapes (if they exist) for different physical parameters.

In the numerical experiments we describe below, we choose to fix the contact points between the fluid and the electrodes (i.e., the values of a_1 and a_2 are fixed) and α and to search for equilibrium solutions satisfying the boundary condition (2.18) by incorporating a motion by curvature along the normal-type algorithm described below. We note that this procedure does not preserve volume, and a value of the final volume is obtained at equilibrium. Different values of α will yield different volumes. An iteration on α and the addition of a volume constraint can be used if desired, as was done in the finite element calculations of Ramos and Castellanos (1993). We describe such results based on our methods in a later section.

The algorithm for finding equilibrium shapes is as follows:

1. Prescribe the physical parameters E_b , ε_p , B , and α and pick the values of a_1 and a_2 which define the fixed wetted area on the lower and upper plate,

respectively.

2. Prescribe an initial shape S_0 defined on a discrete set of mesh or marker points. Each of the two points of S_0 on the upper and lower plate are not allowed to move.
3. Solve for E_τ and E_ν using the boundary integral methods described in preceding sections.
4. Calculate the quantity

$$(6.1) \quad \left(\frac{1}{R_1} + \frac{1}{R_2} \right) + E_b \left[\frac{1}{2} \frac{\varepsilon}{\varepsilon_0} (E_\tau^2 - E_\nu^2) \right]_1^0 + Bz - \alpha = 0$$

at each of the marker points.

5. Move marker points along the interior normal. They are moved for a distance proportional to the quantity (6.1).
6. The new position for the marker points provides a new shape S . Apply a least squares method to derive an equation for the new shape by approximating r as a polynomial P_7 of degree 7 in z . The coefficients of P_7 are constrained by bounds. In addition, this polynomial meets the requirement that its graph passes through the top and bottom points.
7. With a new smooth shape computed, the iteration procedure is repeated by going back to step 3 of the algorithm.

Remark. The middle term in (6.1) can be simplified by writing

$$(6.2) \quad E_b \left[\frac{1}{2} \frac{\varepsilon}{\varepsilon_0} (E_\tau^2 - E_\nu^2) \right]_1^0 = \frac{E_b}{2} (1 - \varepsilon_p) (E_\tau^2 + \varepsilon_p E_{\nu,1}^2).$$

This quantity is positive if $\varepsilon_0 > \varepsilon_1$ and negative if $\varepsilon_0 < \varepsilon_1$; the latter case is more representative of physical situations where the outside surrounding phase is air or a gas. Thus the stabilizing effect of electric fields in such situations is readily apparent.

The iteration is stopped when either of the following occurs:

- Denote by S_r the shape obtained at step r of the iteration. If the distance between S_r and S_p is smaller than a certain set tolerance for all $r_0 \leq r$, $p \leq r_0 + 100$, then we assume that we have found an equilibrium position, S_{r_0} . We also check whether we can reduce the quantity (6.1) below a certain tolerance level.
- The shape tends to collapse into two parts. There is a topological transition. In that case, the surface tension caused the shape to collapse, and the electric stress was not strong enough to counteract that effect. The ultimate shape of the fluid at equilibrium has more than one connected component.
- The shape tends to expand radially to infinity. In that case, the electric stress is dominant and cannot be counteracted by surface tension forces and the pressure term α . The simulation suggests that in such cases, there is no equilibrium shape, for that value of α , that extends from wall to wall and that passes through the given top and bottom points.

6.1. The minimal energy solution. We present a first set of numerical results corresponding to the pressure $\alpha = 0$. These results are of a rather theoretical nature, because they are hard to obtain physically. However, they provide several test examples: in the absence of electric fields, it is possible to find shapes at equilibrium by means of independent and straightforward methods.

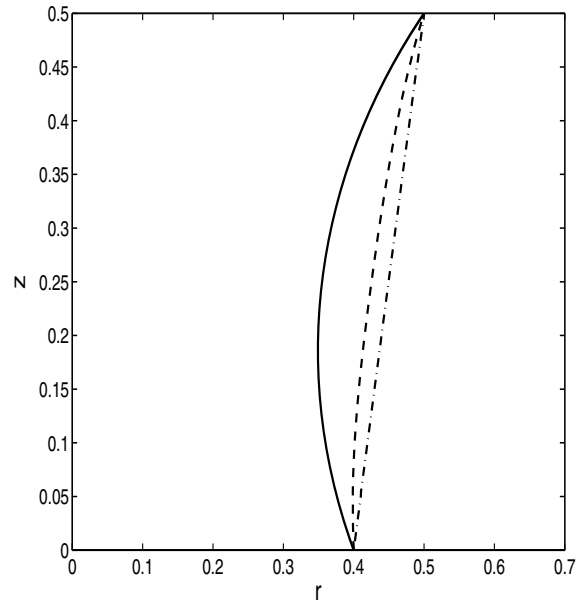


FIG. 3. *Minimal energy equilibrium shapes in the absence of an electric field. The initial curve is the straight line segment, the curve in the middle is found after 50 iterations, and the final curve is found after 200 iterations.*

6.1.1. The case where the electric effects are absent. Euler was the first to study this case. In the absence of gravity, $B = 0$, either there exists a piece of catenary with equation

$$(6.3) \quad r = C \cosh\left(\frac{z-D}{C}\right), \quad C > 0,$$

passing through the two fixed points at the top and bottom, and in that case the equilibrium shape is given by that piece of catenary, or coefficients C and D allowing the catenary to pass through the two fixed points do not exist, in which case there is no connected equilibrium shape. Note that the second case corresponds to the physical situation where the top and bottom points are “too close” to the z -axis, and the liquid bridge collapses. Note also that the coefficients C and D have to be sought numerically.

In a first example, we fixed the bottom point at $(0.4, 0)$ and the top point at $(0.5, 0.5)$. The initial shape is the line segment joining these two points, which is the dashed-dotted line in Figure 3. The dashed curve is the boundary of the approximate shape after 50 iterations. The solid curve is the piece of catenary connecting the two points. Past 200 iterations, it is not possible to tell the difference, by looking at a plot with the same resolution, between the piece of catenary and the computed shape. It was checked that the discrete L^2 norm of the difference in the r -coordinates between the marker points and points on the exact equilibrium shape curve with the same z -coordinate was less than 10^{-4} .

In a second example, we fixed the bottom point at $(0.3, 0)$ and the top point at $(0.4, 0.5)$. The initial shape is the line segment joining these two points, which is the dashed-dotted curve in Figure 4. No connected equilibrium exists in this case, and

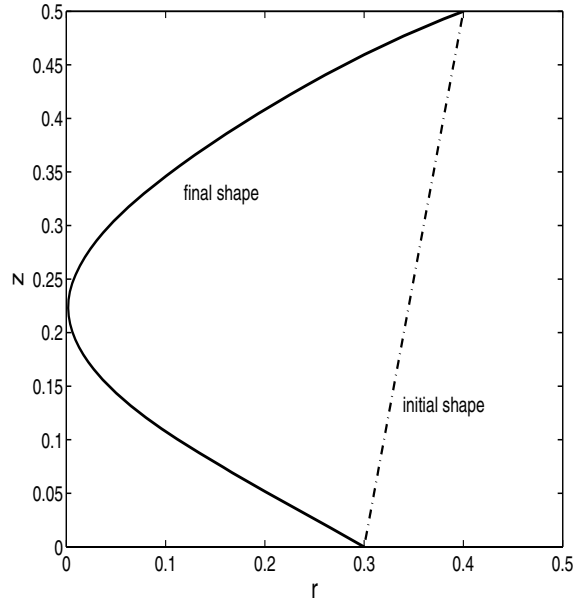


FIG. 4. A collapsing bridge through motion by curvature in the absence of an electric field. No connected minimal energy equilibrium shape is possible.

no real C and D can be found such that the curve defined by (6.3) passes through $(0.3, 0)$ and $(0.4, 0.5)$. After some 520 iterations, the updated shape intersects the z -axis, indicating that the search for connected equilibrium shapes has failed.

6.1.2. The cylindrical equilibrium shape. If S is a vertical line segment, the electric potential V can be found in closed form and is $V = 2z$. If the fixed top and bottom points lie on the same vertical line, for any value of $\varepsilon_0, \varepsilon_1$ such that $\varepsilon_0 < \varepsilon_1$, there is a choice of E_b making the cylinder passing through the two fixed points an equilibrium shape with $\alpha = 0$. This value is

$$(6.4) \quad E_b = \frac{1}{2a_0(\varepsilon_p - 1)},$$

where a_0 is the radius of the cylinder. In addition, if these cylinders are wide enough, they are stable equilibrium shapes. To test our search for equilibrium positions, we pick the values,

$$(6.5) \quad \varepsilon_p = 2, \quad E_b = 1, \quad a_0 = .5,$$

and we start with the initial shape,

$$r = .5 + .05 \sin(4\pi z).$$

The equilibrium shape is the cylinder $r = .5$ for the parameters (6.5). In Figure 5, we plot the initial shape, which is the most curved one, and also the shapes after 30, 60, 90, and 110 iterations using our algorithm. The contours converge to a segment line. The last plotted contour after 110 iterations is indistinguishable from a vertical line segment. Any additional iteration did not alter the segment line, although the coefficients of P_7 did not converge.

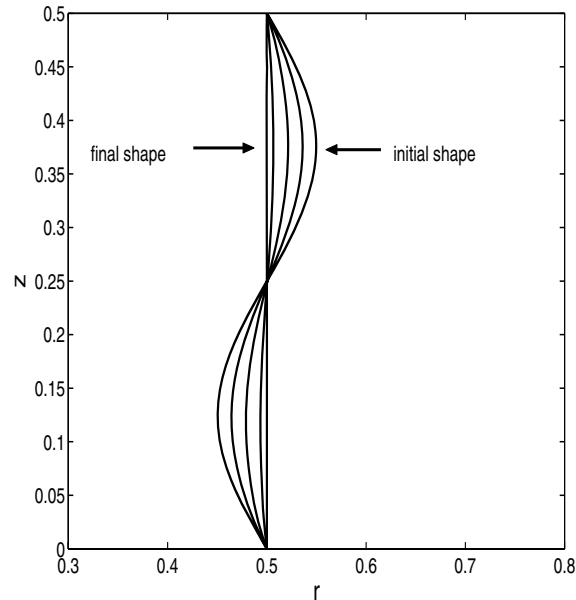


FIG. 5. *Equilibrium shape calculation in the presence of an electric field; $\varepsilon_p = 2$, $E_b = 1$. The initial shape is the most curved one, and it gradually evolves into the cylinder of radius 0.5.*

6.1.3. More interesting cases. In this section we obtain new zero pressure equilibrium shapes in regimes where there is a balance between electric and capillary stresses. In a first example, we fix the top and bottom points with the values $a_1 = .3$, $a_2 = .2$. The initial shape is the line segment connecting these two points. Without the aid of an electric field, the corresponding liquid bridge would collapse due to capillary forces. We now pick

$$\varepsilon_p = 2, \quad E_b = 1.44.$$

After 130 iterations, changes in iterated shapes are minimal, but it appears that there is still a slight oscillation about the equilibrium position. This oscillation can be eliminated, to graphical precision, by choosing a smaller constant of proportionality in step 3 of our algorithm. The computed equilibrium position is depicted in Figure 6.

Results from another numerical simulation show that a value of $E_b = 1.21$ is not strong enough in this case to prevent capillary collapse. As the value of E_b is increased, however, we find convex equilibrium shapes. For example, with the values

$$\varepsilon_p = 2, \quad E_b = 2.89$$

and the same initial shape as in the preceding case, the computed shape converges after about 500 iterations. We plot it in Figure 7.

For values of $E_b = 3.61$ or higher, no zero pressure equilibrium could be reached. The electric stress was just too strong to be compensated by capillary forces. We note that in practice no such physical phenomenon arises due to the adjustment of the pressure jump across the interface which is proportional to α .

6.1.4. Adding the effect of gravity. If the Bond number B is small, the effects of gravity are negligible to leading order. If B grows too large, for fixed

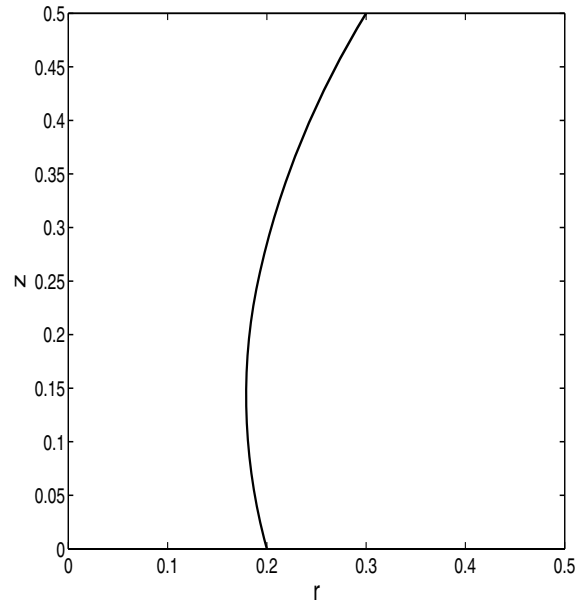


FIG. 6. *Stabilization of a liquid bridge by an electric field. Minimal energy equilibrium for $\varepsilon_p = 2$, $E_b = 1.44$. Converged solution shown after 130 iterations.*

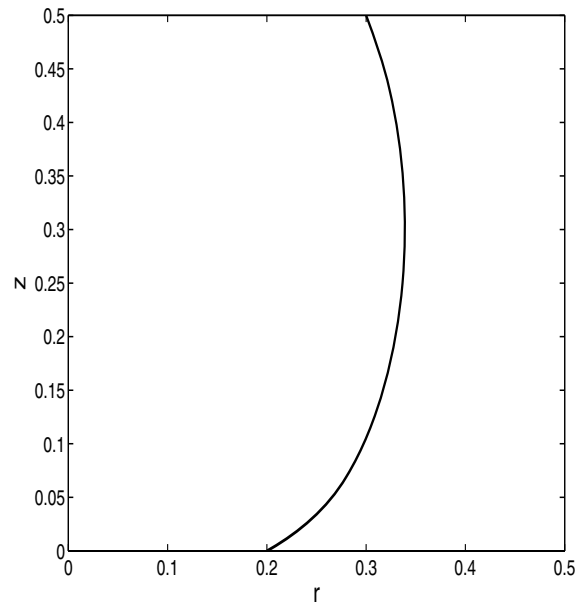


FIG. 7. *A convex equilibrium minimal energy shape obtained by the application of a stronger electric field; $E_b = 2.89$.*

values of the other parameters, the bridge collapses under its own weight. In what follows, we present simulations in regimes where the electric stresses, capillary forces, and gravity are equally important and compete in determining the final equilibrium

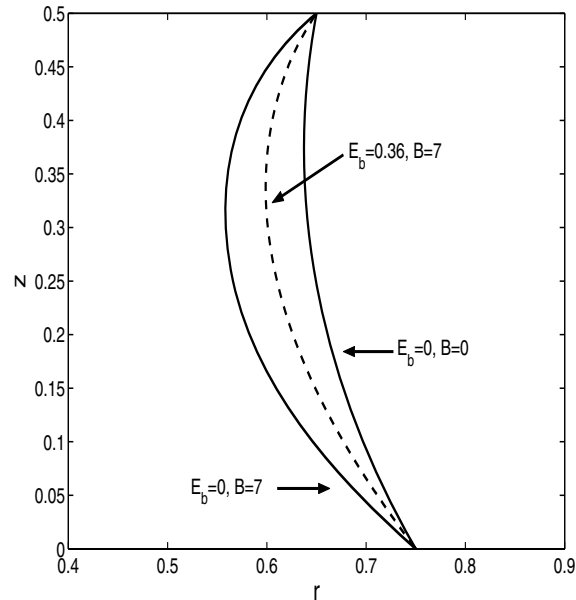


FIG. 8. The equilibrium shape on the left is obtained in presence of gravity ($B = 7$); the equilibrium shape on the right is obtained in absence of gravity.

configurations. To set the stage, we ignore the electric field and take

$$B = 7, \quad E_b = 0,$$

while the bridge radius at the lower plate is $a_1 = 0.75$ and at the upper plate is $a_2 = 0.65$. For these values a zero pressure ($\alpha = 0$) equilibrium shape is obtained and is shown in Figure 8 as the innermost solid curve. The outermost solid curve is the piece of catenary passing through the two fixed points, that is, the equilibrium shape obtained in the absence of gravity, which is included here for the sake of comparison. We are not aware of a closed form solution for the equilibrium shape in the case where B is nonzero. However, it is well known that if the equation of the boundary is in the form $r(z)$, then r satisfies the following boundary value problem, derived from the formula (2.19) for the mean curvature:

$$r'' = Bz(1 + r'^2)^{\frac{3}{2}} + \frac{1 + r'^2}{r},$$

$r(0), \quad r\left(\frac{1}{2}\right)$ are given boundary data.

This boundary value problem can be efficiently solved numerically for the values of B , $r(0)$, and $r(\frac{1}{2})$ of our example. The contour computed by this alternative method resembles so closely the calculated contour obtained by our motion by curvature algorithm that we do not superimpose a plot of it here.

In the next simulation, we want to demonstrate how an electric field enhances the stability of equilibrium solutions. The value for $B = 7$ is the same as above. In addition, we pick

$$\varepsilon_p = 2, \quad E_b = .36,$$

and we plot also in Figure 8 the resulting equilibrium shape: it appears as the dashed line. The electric field acts to reduce the curvature of the equilibrium shape, and hence acts in a stabilizing manner.

6.2. Volume preserving equilibrium shapes. In this section, we compute equilibrium shapes satisfying two constraints: (i) the points on the top and bottom plates are imposed and fixed, and (ii) volume is conserved. As discussed earlier, the final pressure difference α is then an unknown, and it has to be calculated as part of the solution. The final volume obtained by application of our search algorithm for a fixed α is an increasing function of α : this is because of the motion along the normal vector. For finding volume preserving equilibrium shapes and corresponding pressures at equilibrium, we make two initial guesses for α , and then iterate on α using the secant method, to find the value α^* that will preserve a given initial volume.

In the first experiment, we fix the points on the top and bottom plates to be at $r = .07$ and take $B = 0$. We seek equilibrium shapes that preserve the initial volume given by the equation

$$(6.6) \quad r = .07(1 - .1 \sin(2\pi z))$$

and which is equal to $6.75538 \cdot 10^{-3}$, correct to 6 decimals. This initial configuration lies below the Plateau limit where no stable equilibrium exists for $E_b = 0$. The numerical search for equilibrium fails, as predicted by the theory. We now introduce the effects of an electric field using the values $\varepsilon_p = 2$, $E_b = 16$. Note that the value chosen for E_b is a value that yields an equilibrium position for a cylinder passing through the closest point to the z -axis on the curve of (6.6), that is, a cylinder of radius 0.063. The search for an equilibrium shape and final pressure was successful, and the computed value for α^* is -17.1732731713385 . We conclude that equilibrium is reached after some 300 iterations, because no change in shape is observed if the algorithm is continued for another 50 iterations. The shape at equilibrium is plotted in Figure 9.

The computed equilibrium shape has the desired volume, up to 6 decimals. The visual difference in shape between the final curve in the algorithm and the curve (6.6) is slight.

In a second simulation, we fix the points on the top and bottom plates to be at $r = .3$. We seek to preserve the volume occupied by the corresponding cylinder, that is, approximately, 0.1413716. This time we are well above the Plateau limit allowed for gravity to be present with the Bond number $B = 30$. In a first run, we compute an equilibrium shape in the absence of electric forces and obtain the familiar amphora-like shape; the final pressure value is $\alpha^* = 10.7302756813844$. We then apply an electric field using the values $\varepsilon_p = 2$, $E_b = 10$. The final shape at equilibrium is much flatter in this case, and the configuration is closer to an undisturbed cylinder due to the stabilizing effects of the electric field. Equilibrium shapes in each case are plotted in Figure 10. The final computed value for α^* is -9.2584080738938 . This calculation verifies that the electric field acts to offset the destabilizing effects of gravity through stabilizing electric stresses at the interface. This is in agreement with results from experiments (see Gonzalez et al. (1989) and Ramos, Gonzalez, and Castellanos (1994)), as well as linear stability studies of the governing equations (see Pelekasis, Economou, and Tsamopoulos (2001)).

7. Conclusions. We have introduced and implemented efficient and highly accurate boundary integral methods which can be used to solve electrified liquid bridge

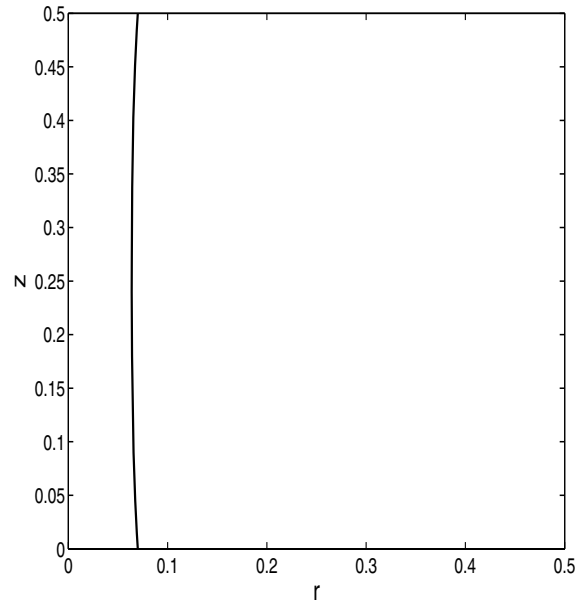


FIG. 9. *Stabilization of a thin liquid bridge by an electric field; $\varepsilon_p = 2$, $E_b = 16$.*

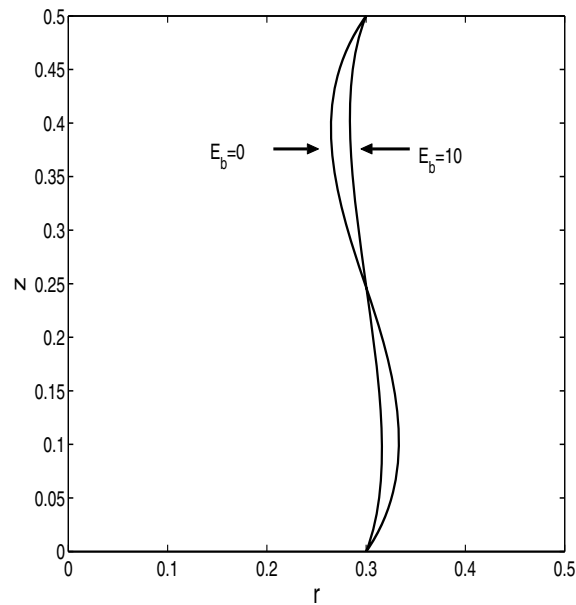


FIG. 10. *Effect of electric fields on amphora-like configurations obtained in the presence of gravity. The equilibrium shape is straighter when an electric field is applied; $\varepsilon_p = 2$, $E_b = 10$.*

problems. The presence of bounding electrodes introduces the need to develop fast and accurate methods for the calculation of series representations of the Green's function in axisymmetric geometries. We demonstrate how to do this using Ewald's method and perform extensive tests that establish the accuracy of our summation compared

to keeping a large number of terms in the conventional sum (or, more precisely, their gradients). For example, we show numerically that for a desired 12-digit accuracy, the conventional sum would require over 7×10^4 terms, whereas our Ewald sums obtain the same accuracy with less than 10 terms.

The accuracy and efficiency of the Green's function calculation is incorporated into the numerical solution of a boundary integral equation for the electric field components on the free interface and the ultimate use of the computed stresses in the determination of equilibrium shapes. We present two types of solutions: minimum energy and volume preserving solutions. Both are calculated through a transient algorithm that involves motion by curvature. Equilibrium shapes in the presence (or absence) of electric fields and gravity are computed for a range of physical parameters. Our results are in complete agreement with alternative finite element calculations and linear theory, which predict a stabilization of the flow in the presence of axial electric fields. The stability in the present context manifests itself either by flattening the interface of equilibrium shapes for parameter regimes above the Plateau limit or by preventing collapse in parameter regimes below the Plateau limit, provided the strength of the applied field is strong enough. Finally, we note that all computed equilibrium shapes are appropriate for both viscous and inviscid fluids, as we have only considered the static problem. The addition of a boundary integral equation for the fluid potential ϕ and the computation of time evolving states in the inviscid case is the subject of ongoing research.

Appendix. We first propose to prove that integral equation (3.7) is well posed. Suppose that a density μ defined on S satisfies the homogeneous equation

$$(7.1) \quad \frac{1}{2}(1 + \varepsilon_p)\mu - (1 - \varepsilon_p) \int_S \frac{\partial H}{\partial \nu_{r_0, z_0}} \mu(r, z) ds(r, z) = 0.$$

Notice that we can integrate the identity (7.1) in the variables (r_0, z_0) , and using the identity $\int_S \frac{\partial H}{\partial \nu_{r_0, z_0}} ds(r_0, z_0) = \frac{1}{2}$, we arrive at

$$(7.2) \quad \int_S \mu(r, z) ds(r, z) = 0.$$

Define the function

$$(7.3) \quad f(r_0, z_0) = \int_S H(r, z, r_0, z_0) \mu(r, z) ds(r, z).$$

Note that due to the definition of f and (7.1), we have

$$(7.4) \quad \Delta f = 0, \quad 0 \leq r < S(z, t), \quad 0 < z < \frac{1}{2},$$

$$(7.5) \quad \Delta f = 0, \quad S(z, t) < r < \infty, \quad 0 < z < \frac{1}{2},$$

$$(7.6) \quad [f]_1^0 = 0,$$

$$(7.7) \quad \left[\frac{\varepsilon}{\varepsilon_0} \nabla f \cdot \nu \right]_1^0 = 0.$$

Since

$$H(r, z, r_0, z_0) = -\log r + O\left(\frac{1}{r}\right),$$

as r grows large, recalling (7.2), we infer that

$$f(r_0, z_0) = O\left(\frac{1}{r_0}\right),$$

as r_0 grows large. Similarly,

$$\frac{\partial H(r, z, r_0, z_0)}{\partial r} = -\frac{1}{r} + o\left(\frac{1}{r}\right)$$

and

$$\frac{\partial f(r_0, z_0)}{\partial r_0} = o\left(\frac{1}{r_0}\right).$$

In view of (7.4)–(7.7), applying Green’s theorem to $f \frac{\partial f}{\partial z}$ in a rectangle in the r - z plane such that two opposite sides lie on the planes $z = 0$ and $z = 1/2$ and the other two sides tend to infinity, we derive

$$(7.8) \quad \varepsilon_p \int_{\mathcal{R}_1} |\nabla f|^2 + \int_{\mathcal{R}_0} |\nabla f|^2 = 0,$$

where \mathcal{R}_1 is the region inside S , and \mathcal{R}_0 is the corresponding exterior region. Since $\varepsilon_p \neq 0$, ∇f has to be zero in \mathcal{R}_0 and in \mathcal{R}_1 . Now, using the usual jump condition for the derivatives of single layer potentials, we infer that $\mu = 0$.

We have thus proved uniqueness for the linear integral equation of the second kind (3.7). Note that, up to a constant, the left-hand side of this equation appears in the classical form “identity plus compact.” According to Theorem 10.9 in Kress (1999), we just need to verify that our sequence of operators that approximate the integral operators involved in the left-hand side of (3.7) is pointwise convergent and collectively compact. Our approximated operators are obtained by applying converging numerical quadratures. As explained in Theorem 12.8 in Kress (1999), collective compactness is guaranteed when integrating against continuous kernels. More care has to be taken for the integration kernel exhibiting a logarithmic singularity. We seek to verify the necessary condition 12.14 in Kress (1999). That condition ensures collective compactness for a sequence of approximating operators derived by quadrature, converging to a weakly singular integral operator. In our case, we found the quadrature coefficients $\beta_k^{(n)}(t)$ for the integral,

$$(7.9) \quad \int_0^1 \log|t-v|g(v)dv \simeq \sum_{k=1}^{n-1} \beta_k^{(n)}(t)g\left(\frac{k}{n}\right).$$

With these notations, Kress’s necessary condition 12.14 can be expressed as

$$(7.10) \quad \limsup_{u \rightarrow t} \sum_n \sum_{k=1}^{n-1} |\beta_k^{(n)}(t) - \beta_k^{(n)}(u)| = 0.$$

We chose to derive the $\beta_k^{(n)}(t)$ as follows:

- For $2 \leq k \leq n - 3$, g was approximated on $[\frac{k}{n}, \frac{k+1}{n}]$ by the mean of the quadratic polynomial interpolating g at $\frac{k-1}{n}, \frac{k}{n}, \frac{k+1}{n}$ and the quadratic polynomial interpolating g at $\frac{k}{n}, \frac{k+1}{n}, \frac{k+2}{n}$.

- g was approximated on $[0, \frac{2}{n}]$ by the quadratic polynomial interpolating g at $\frac{1}{n}, \frac{2}{n}, \frac{3}{n}$.
- g was approximated on $[\frac{n-2}{n}, 1]$ by the quadratic polynomial interpolating g at $\frac{n-3}{n}, \frac{n-2}{n}, \frac{n-1}{n}$.

It follows that our quadrature rule is convergent and the $\beta_k^{(n)}$ satisfy the estimate

$$(7.11) \quad |\beta_k^{(n)}(t) - \beta_k^{(n)}(u)| \leq M \int_{\frac{k-2}{n}}^{\frac{k+2}{n}} |\log|t-v| - \log|t-u||dv,$$

where the constant M is independent of k, n, t , and u . Thus to ensure (7.10), we just need to verify that

$$(7.12) \quad \lim_{u \rightarrow t} \int_0^1 |\log|t-v| - \log|u-v||dv = 0,$$

which is elementary.

REFERENCES

- M. ABRAMOWITZ AND I. STEGUN, EDs. (1992), *Handbook of Mathematical Functions with Formulas, Graphs, and Mathematical Tables*, Dover, New York.
- M. BORN AND K. HUANG (1954), *Dynamical Theory of Crystal Lattices*, Oxford University Press, Oxford, UK.
- C. L. BURCHAM AND D. A. SAVILLE (2000), *The electrohydrodynamic stability of a liquid bridge: Microgravity experiments on a bridge suspended in a dielectric gas*, J. Fluid Mech., 405, pp. 37–56.
- P. G. DRAZIN AND W. H. REID (1981), *Hydrodynamic Stability*, Cambridge University Press, Cambridge, UK.
- P. P. EWALD (1921), *Die Berechnung optischer und elektrostatischer Gitterpotentiale*, Ann. Phys., 64, pp. 253–268.
- J. EGGERS (1997), *Nonlinear dynamics and breakup of free-surface flows*, Rev. Modern Phys., 3, pp. 865–929.
- S. GAUDET, G. H. MCKINLEY, AND H. A. STONE (1996), *Extensional deformation of liquid bridges*, Phys. Fluids A, 8, pp. 2568–2579.
- H. GONZALEZ AND A. CASTELLANOS (1993), *The effect of residual gravity on the stability of liquid columns subjected to electric fields*, J. Fluid Mech., 249, pp. 185–206.
- H. GONZALEZ, F. M. J. MCCLUSKEY, A. CASTELLANOS, AND A. BARRERO (1989), *Stabilization of dielectric liquid bridges by electric fields in the absence of gravity*, J. Fluid Mech., 206, pp. 545–561.
- T. Y. HOU, J. S. LOWENGRUB, AND M. J. SHELLEY (2001), *Boundary integral methods for multi-component fluids and multiphase materials*, J. Comput. Phys., 169, pp. 302–362.
- J. D. JACKSON (1962), *Classical Electrodynamics*, Wiley, New York.
- R. KRESS (1999), *Linear Integral Equations*, 2nd ed., Appl. Math. Sci. 82, Springer-Verlag, New York.
- L. D. LANDAU AND E. M. LIFSHITZ (1987), *Fluid Mechanics. Course of Theoretical Physics, Volume 6*, 2nd ed., Butterworth Heinemann, Burlington, MA.
- C. M. LINTON (1998), *The Green's function for the two-dimensional Helmholtz equation in periodic domains*, J. Engrg. Math., 33, pp. 377–402.
- C. M. LINTON (1999), *Rapidly convergent representations for Green's functions for Laplace's equation*, R. Soc. Lond. Proc. Ser. A Math. Phys. Eng. Sci., 455, pp. 1767–1797.
- G. H. MCKINLEY AND A. TRIPATHI (2000), *How to extract the Newtonian viscosity from capillary breakup measurements in a filament rheometer*, J. Rheol., 44, pp. 653–670.
- D. T. PAPAGEORGIU (1995a), *On the breakup of viscous liquid threads*, Phys. Fluids, 7, pp. 1529–1544.
- D. T. PAPAGEORGIU (1995b), *Analytical description of the breakup of liquid jets*, J. Fluid Mech., 301, pp. 109–132.
- D. T. PAPAGEORGIU (1996), *Description of jet breakup*, in Advances in Multi-fluid Flows, Y. Y. Renardy, A. C. Coward, D. T. Papageorgiou, and S.-M. Sun, eds., SIAM, Philadelphia, pp. 171–198.
- D. T. PAPAGEORGIU AND M. VANDEN-BROECK (2004), *Large amplitude capillary waves in electrified fluid sheets*, J. Fluid Mech., 508, pp. 71–88.

- N. A. PELEKASIS, K. ECONOMOU, AND J. A. TSAMOPOULOS (2001), *Linear oscillations and stability of a liquid bridge in an axial electric field*, Phys. Fluids, 13, pp. 3564–3581.
- J. PLATEAU (1873), *Statique Experimentale et Theoretique des Liquides Soumis aux Seules Forces Moleculaires*, Gauthier-Villars, Paris.
- C. POZRIKIDIS (2001), *Interfacial dynamics for Stokes flow*, J. Comput. Phys., 169, pp. 250–301.
- A. RAMOS AND A. CASTELLANOS (1993), *Bifurcation diagrams of axisymmetric liquid bridges of arbitrary volume in electric and gravitational axial fields*, J. Fluid Mech., 249, pp. 207–225.
- A. RAMOS, H. GONZALEZ, AND A. CASTELLANOS (1994), *Experiments on dielectric liquid bridges subjected to axial electric fields*, Phys. Fluids, 6, pp. 3206–3208.
- L. RAYLEIGH (1878), *On the instability of jets*, Proc. London Math. Soc., 10, pp. 4–13.
- L. RAYLEIGH (1892), *On the stability of a cylinder of viscous liquid under capillary force*, Phil. Mag., 34, p. 145.
- A. ROTHERT, R. RICHTER, AND I. REHBERG (2001), *Transition from symmetric to asymmetric scaling function before drop pinch-off*, Phys. Rev. Lett., 87, 084501.
- A. ROTHERT, R. RICHTER, AND I. REHBERG (2003), *Formation of a drop: Viscosity dependence of three flow regimes*, New J. Phys., 5, article 59.
- B. S. TILLEY, P. G. PETROPOULOS, AND D. T. PAPAGEORGIOU (2001), *Dynamics and rupture of planar electrified liquid sheets*, Phys. Fluids, 13, pp. 3547–3563.